

# Phonons in highly-crystalline mesoporous silicon: the absence of phonon-softening upon structuring silicon on sub-10 nanometer length scales

Tommy Hofmann<sup>a</sup>, Danny Kojda<sup>a</sup>, Haider Haseeb<sup>a</sup>, Dirk Wallacher<sup>a</sup>,  
Oleg Sobolev<sup>c,d</sup>, Klaus Habicht<sup>a,b</sup>

<sup>a</sup>*Helmholtz-Zentrum Berlin für Materialien und Energie GmbH, Hahn-Meitner Platz  
1, D-14109 Berlin, Germany*

<sup>b</sup>*Institut für Physik und Astronomie, Universität Potsdam, Karl-Liebknecht-Str. 24-25,  
D-14476 Potsdam, Germany*

<sup>c</sup>*Institut für Physikalische Chemie, Universität Göttingen, Tammannstr. 6, D-37077  
Göttingen, Germany*

<sup>d</sup>*Heinz Maier-Leibnitz Zentrum (MLZ), Technische Universität München, Lichtenbergstr.  
1, D-85748 Garching, Germany*

---

## Abstract

This article presents inelastic thermal neutron scattering experiments probing the phonon dispersion in mesoporous silicon with pores 8 nm across. Scattering studies reveal the energy-momentum relation for transverse and longitudinal phonons along the high symmetry directions  $\overline{\Gamma L}$ ,  $\overline{\Gamma K}$  and  $\overline{\Gamma X}$  in the Brillouin zone. The dispersion up to phonon energies of 35 meV unambiguously proves that the phonon group velocities in highly-crystalline silicon are not modified by nanostructuring down to sub-10 nanometer length scales. On these length scales, there is apparently no effect of structuring on the elastic moduli of mesoporous silicon. No evidence can be found for phonon-softening in topologically complex, geometrically disordered mesoporous silicon putting it in contrast to silicon nanotubes and nanoribbons.

*Keywords:* mesoporous silicon, inelastic neutron scattering, phonon dispersion, phonon-softening, elasticity, thermoelectric material

---

## 1. Introduction

Inorganic and organic thermoelectric materials exploit the Peltier and Seebeck effect to directly convert thermal energy into electrical energy and *vice-versa* [12].  $\text{Bi}_2\text{Te}_3$  and  $\text{PbTe}$  are classical thermoelectric materials (TE) with market-ready technological applications [41, 23] but have the obvious drawback of not being environmental friendly. More contemporary TE materials are skutterudites [32], clathrates, half-Heusler alloys, thermoelectric oxides and

---

*URL:* [tommy.hofmann@helmholtz-berlin.de](mailto:tommy.hofmann@helmholtz-berlin.de) (Tommy Hofmann)

nanostructured systems [38]. However, most of these state-of-the-art TE materials are not yet efficient enough, too expensive, not scalable in synthesis or too toxic to play a key role in a future, sustainable and green energy infrastructure. The development of novel TE's is one pillar of modern energy research next to photovoltaic, catalysis and fuel cell technologies. Scientists and material engineers are heavily guided by the figure of merit  $zT = \frac{\sigma S^2}{\kappa_{ph} + \kappa_{el}} T$  in their quest for novel materials. It manifests the insight that a high performing TE should provide at operating temperature  $T$  a high electrical conductivity  $\sigma$ , a high Seebeck coefficient  $S$  and low electronic and lattice thermal conductivities  $\kappa_{el/ph}$ . The material properties that define  $zT$  are strongly and not necessarily favorably correlated, e. g., by the Wiedemann-Franz law or the Mott equation [19]. Thus find the perfect phonon-glass and electron crystal [37, 29] for TE applications is a challenging optimization problem. Doping and electronic band structure engineering [30] are intensively studied to optimize for instance the power factor  $\sigma S^2$  whereas nanostructuring and phonon-dispersion engineering [18, 27, 20] are considered approaches to impair the lattice thermal conductivity  $\kappa_{ph}$ .

The effect of nanostructuring on  $\kappa_{ph}$  is typically probed in macroscopic thermal conductivity measurements. Increased phonon boundary scattering at interfaces is the accepted theoretical explanation for modified thermal conductivities in nanostructured materials compared to the respective bulk systems. Phonon-softening induced by structuring is also considered. It is a more subtle effect [16] and experimental evidence remains mostly elusive [35] for monolithic samples but is confirmed to some extent for individual nanowires [40, 42]. Experimental, microscopic studies that directly probe phonon scattering rates or the phonon dispersion modification upon nanostructuring are missing.

Anodized silicon with 2 nm to 200 nm wide pores is one form of nanostructured silicon that offers easy and scalable synthesis routes. Commonly referred to as mesoporous silicon (pSi) it is the perfect model system to study the effect of nanostructuring on the phonon dispersion in an academic as well as technological relevant model system. Its highly-crystalline nature [15] makes it particularly suited for structural and dynamical scattering studies.

It is necessary to employ a suite of experimental techniques that probe different length scales in the material to achieve a comprehensive understanding of lattice vibrations in pSi [1, 2, 16]. One is well advised to carefully distinguish between the properties of the nanostructured silicon itself and the properties of the effective medium that includes crystalline silicon and vacant pore space. In other words, it is essential to distinguish between properties on microstructural and macrostructural length scales.

Inelastic thermal neutron scattering provides microscopic information about phonons across the entire Brillouin zone. It must be considered solely sensitive to the properties of the silicon skeleton when the probed phonon wavelengths become smaller than the length scale of structuring. However, the experimental demand for macroscopic amounts of nanostructured material ( $\approx 1 \text{ cm}^3$ ) with well-aligned crystallographic orientation is a formidable obstacle.

This article presents the phonon dispersion of pSi with pores roughly  $2R \approx 8 \text{ nm}$

across at a porosity of  $\phi \approx 50\%$  that is obtained by thermal neutron scattering experiments. It is a direct continuation of the inelastic cold neutron scattering study presented in Ref. [16]. The recent data are discussed in the context of the influence of nanostructuring on the elastic properties of a crystalline material and put into perspective of contemporary studies on this subject [13, 11, 1].

## 2. Experiment

### 2.1. Samples

The synthesis of pSi relies on the anodization of single-crystalline, p- or n-doped silicon wafers in electrolytes that contain hydrofluoric acid (HF) [44, 7, 33]. The most important control parameters of this anodization process are the HF concentration, current density, illumination and etching time. With the appropriate resistivity and crystallographic orientation of the used silicon wafers, it is possible to control pore sizes, porosity and inter-connectivity of the etched pore networks.

Samples for this study are synthesized by electrochemical etching of p-type [001] silicon wafers with a resistivity of  $0.01\text{-}0.02 \text{ }\Omega\text{cm}^{-1}$ . Wafers are anodized in a 4 : 6 electrolyte composed of HF (48 vol-%) and ethanol (99 vol-%) utilizing an etching current density of  $j = 12 \text{ mA/cm}^2$ . After 4h of etching, an increased current density of  $j = 216 \text{ mA/cm}^2$  is applied for 40s to detach  $160 \text{ }\mu\text{m}$  thick, self-supporting membranes with a diameter of roughly 5 cm from the bulk wafers.

38 membranes are etched under identical anodization conditions for the scattering studies. Prior to the scattering experiments, the membranes are laser-cut along the crystallographic [110] and  $\bar{1}\bar{1}0$  directions. A stack  $30 \times 30 \times 6 \text{ mm}^3$  in size is assembled in a sealed sample cell under a dry nitrogen atmosphere with a crystallographic misalignment of less than  $0.5^\circ$  [16]. An identical stack of 38 stack of thin bulk silicon (bSi) plates is assembled for the bulk reference measurements. The highly-crystalline nature of the synthesized membranes is documented in reference [15].

### 2.2. Characterization

The etched pSi membranes are extensively characterized by scanning electron microscopy and nitrogen  $N_2$  sorption isotherms, which provide information of the morphological properties of the samples. We briefly discuss the relevant results of these measurements. More details on the characterization can be found in Ref. [16].

Fig. 1(a) shows a representative  $N_2$  sorption isotherm of a single membrane. It shows at  $T = 77 \text{ K}$  the volumetric liquid- $N_2$  uptake  $f = N/N_0$  in porous silicon upon increasing or decreasing the partial vapor pressure  $P_{red} = P/P_0$ .  $N$  and  $N_0$  are the number of physisorbed  $N_2$  molecules at partial and complete pore filling whereas  $P$  and  $P_0$  refer to the  $N_2$  vapor pressure below and at saturation ( $P_0(77 \text{ K}) = 1013 \text{ mbar}$ ).

The Barrett-Joyner-Halenda analysis [4] of the desorption measurements as depicted in Fig. 1(b) identifies an average pore radius of  $\bar{R} = 4$  nm for the mesoporous membranes. Given for instance pore blocking effects, this might be considered a conservative estimate for the pore size [22, 10, 34]. A specific surface of  $A = 157$  m<sup>2</sup>/g is inferred from a Brunauer-Emmet-Teller analysis [5] of the low pressure part of the isotherm before onset of capillary condensation. Membrane volume and  $N_0$  allow finally a porosity estimate of  $\phi \approx 50\%$ . The SEM micrographs in Fig. 2(a),(b) show the sample top view and cross section illustrating the polygonal pore cross section [9] and the dendritic growth of the pores along the [100] direction. The top view in panel (a) shows a random array of pores without long-range order contrasting highly-ordered mesoporous thin-films synthesized by polymer-templating [26]. It provides a direct route towards a pore size distribution (PSD) for the front (electrolyte exposed) side of the membrane. A dedicated algorithm [24] identifies the polygonal contour lines of the pores and uses the enclosed area to calculate the equivalence radius of a circular pore. The resulting PSD is shown in the inset. Despite an average pore radius comparable with the isotherm result, this PSD should be considered surface and not bulk representative. In particular, close inspection of PSD's obtained from the front and back side of the membrane differ in average radius up to 50% indicating an expected, etching-induced porosity gradient along the [100] direction.

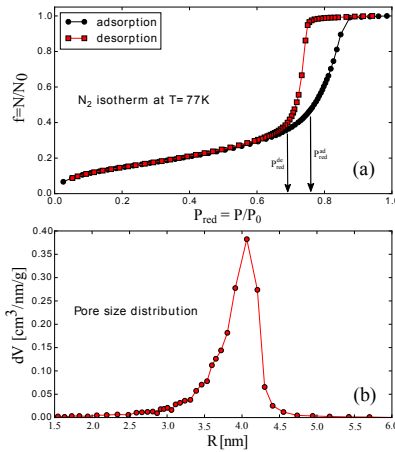


Figure 1: (Color online) (a) N<sub>2</sub> sorption isotherm measured at  $T = 77$  K in pSi. (b) Pore size distribution in pSi estimated from the desorption branch of the N<sub>2</sub> isotherm employing a BJH-analysis. Reprinted from Ref. [16] with permission from Elsevier.

### 2.3. Neutron scattering

Inelastic neutron scattering data are collected with PUMA, a thermal triple-axis spectrometer at the high-flux neutron research reactor FRM II in Garching, Germany. It is designed to probe the scattering function  $S(\vec{Q}, \omega)$  of elementary

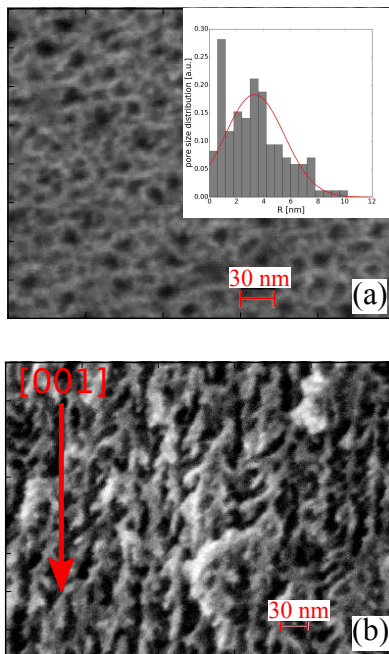


Figure 2: (Color online) SEM micrograph of pSi recorded with a SEM LEO GEMINI microscope employing electron energies of 15 keV: (a) Top view of the pores in etched silicon. The inset illustrates the pore size distribution as inferred from a contrast analysis of the SEM image. (b) Side view of the pores. Reprinted from Ref [16] with permission from Elsevier.

excitations such as phonons and magnons in single-crystalline materials. Depending on the lattice parameters and crystal structure of the system under investigation, excitations with energies up to  $\hbar\omega = 100$  meV and wavevectors of  $|\vec{q}| = 12 \text{ \AA}^{-1}$  can be measured [39].

All scattering experiments are performed at room temperature. Two types of scans are utilized to measure the phonon energy versus phonon wavevector dispersion relation  $\hbar\omega(\vec{q})$  in pSi and bSi along well-defined crystallographic directions. So-called constant-energy scans measure the intensity of scattered neutrons with fixed energy loss for different wavevector transfers  $\vec{q}$ . They are suited to probe the low energy dispersion where the phonon energy  $\hbar\omega$  depends strongly on the probed phonon wavevector  $\vec{q}$ . So-called constant- $\vec{q}$  scans record the neutrons depending on the energy loss  $\hbar\omega$  at fixed wavevector transfer  $\vec{q}$ . They are typically performed closer to the boundary of the Brillouin zone where a weak  $\omega(\vec{q})$  dependence is evident. PUMA measures neutrons with a fixed final wavevector  $|\vec{k}_f| = 4.11 \text{ \AA}^{-1}$  and varies the incident wavevector  $\vec{k}_i$  for the constant- $\vec{q}$  scans. For the constant-energy scans both  $|\vec{k}_i|$  and  $|\vec{k}_f|$  are fixed. Representative scans are shown in Fig. 3.

The neutron scattering experiments are conceived to elucidate phonons along

high symmetry directions in the Brillouin zone of silicon as depicted in Fig. 4. Probed are specifically  $\overline{\Gamma L}$ ,  $\overline{\Gamma K}$  and  $\overline{\Gamma X}$  directions. All information about the phonon dispersion are of course contained within the first Brillouin zone and depend solely on the reduced phonon wavevector  $\vec{q}$  [3]. However, inelastic scattering of neutrons on phonons increases with the absolute wavevector transfer  $\vec{Q} = \vec{Q}_{Bragg} + \vec{q}$  [36] between neutron and lattice. Consequently, phonons are best measured in the highest instrumentally accessible Brillouin zones to maximize scattering intensity and consequently to improve signal-to-noise ratios.

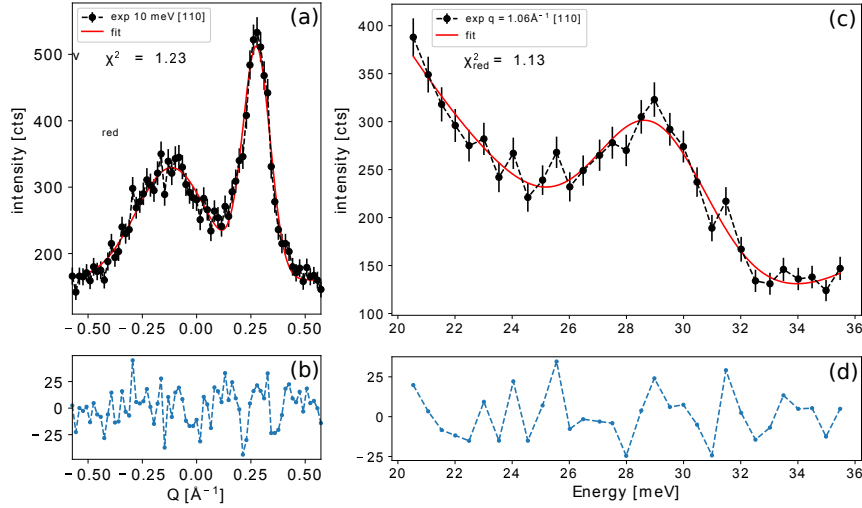


Figure 3: (Color online) (a) A 10 meV transverse phonon becomes evident in a q-scan along the [110] direction that is measured around the 004 Bragg reflection (black symbols). The instrumental configuration of the triple-axis spectrometer PUMA probes the phonon in a defocusing condition ( $q < 0$ ) and a focusing condition ( $q > 0$ ). Non-linear least squares fitting employing two Gaussians is utilized to extract the wave-vector  $q$  of the 10 meV phonon (red line) (c) For a wavevector transfer of  $q = 1.06 \text{ \AA}^{-1}$  the [110] transverse phonon becomes evident in an  $\omega$ -scan for an energy transfer of approximately 28 meV. Non-linear least squares fitting employing one Gaussian and a polynomial background is utilized to extract the energy of the phonon (red line) (b)+(d) Residual between non-linear least squares approximation and the data.

#### 2.4. Data analysis

The arguably most intuitive approach to analytically describe the transverse and longitudinal phonon dispersions along the high symmetry directions of silicon are one-dimensional chain-like models. These models readily predict the collective motions of entire netplanes. Depending on the desired degree of approximation, they account for the interaction between neighboring netplanes up to an arbitrary order that are for instance nearest neighbor and next nearest neighbor interactions. The entire approach, although simplified, bears a striking resemblance to more fundamental Born-Karman calculations [43] and is used

here.

The phonon dispersion for a linear chain of netplanes is given by

$$\omega^2 = \sum_{i=1}^{\infty} D_i (1 - \cos(qia)). \quad (1)$$

Here,  $a$  is the distance between adjacent netplanes,  $\omega$  is the frequency of the phonons, and  $D_i$  encodes the interaction between netplanes.

From Eqn. 1 the sound velocity is inferred in the low  $q$  limit to be

$$v_s = \sqrt{\sum_{i=1}^{\infty} i^2 D_i \frac{a}{2}}. \quad (2)$$

There are three independent components  $c_{ij}$  of the stiffness tensor in crystals with cubic symmetry. These elastic moduli  $c_{11}$ ,  $c_{12}$ , and  $c_{44}$  relate to the sound velocities in the crystallographic directions  $[hkl]$  via the general expression

$$v_{T/L}^{[hkl]} = \sqrt{\frac{f_{T/L}^{[hkl]}(c_{11}, c_{12}, c_{44})}{\rho}}, \quad (3)$$

where  $\rho = 2.33 \text{ gcm}^{-3}$  is the silicon mass density and  $f_{T/L}^{[hkl]}$  are functions of the three independent elastic constants [16]. It is

$$\begin{aligned} f_L^{[100]} &= c_{11} \\ f_T^{[100]} &= c_{44} \\ f_L^{[110]} &= \frac{c_{11} + c_{12} + 2c_{44}}{2} \\ f_T^{[110]} &= c_{44} \\ f_L^{[111]} &= \frac{c_{11} + 2c_{12} + 4c_{44}}{3} \\ f_T^{[111]} &= \frac{c_{11} - c_{12} + c_{44}}{3}. \end{aligned} \quad (4)$$

Knowledge of transverse and longitudinal sound velocities in different crystallographic directions allows employing an optimization scheme [16] to determine directly the three elastic constants or related quantities like Young moduli  $Y^{[hkl]}$ .

For the non-linear least squares approximation of the phonon dispersion (Fig. 5), the limited number of data points necessitates a conservative approach of minimal number of fitting parameters. Consequently, for transverse phonons, the sum in Eqn. 2 is truncated at  $i = 2$  and for longitudinal ones already at  $i = 1$ .

### 3. Results and discussion

It is important for nanostructured materials like pSi to distinguish between micro- and macrostructural properties. Experiments often probe effective quantities averaged and homogenized over length scales  $l$  that are significantly larger than the structuring length  $d$ . In such a case  $l^{-1}d \ll 1$  and experiments do not necessarily provide access to microscopic properties on the nanoscale.

Acoustic transmission spectroscopy [1] is employed to study acoustic sound waves in the limit of long wavelengths  $q \rightarrow 0 \text{ \AA}^{-1}$ , where  $q$  refers to the wavevector of the respective vibrational mode. In the analysis of these experiments, pSi is inherently treated as an effective medium that consists of a single-crystalline silicon skeleton penetrated by nanometer sized pores. The technique provides consequently insights into the porosity dependent sound velocities and elastic properties of the compound material. Brillouin scattering [2] probes phonons close to the center of the Brillouin zone and data analysis again treats pSi as continuum to obtain averaged material properties.

If at all, macroscopic measurements allow inferring microstructural properties only indirectly from more or less complex data modeling [11, 13, 31, 25]. Thermoelectric transport measurements on pSi provide effective thermal conductivities, effective electrical conductivities and effective Seebeck coefficients. Relating these effective quantities to microscopic properties requires at least spatial averaging over interconnected Si-walls and a geometrically complex pore space to properly account for the sample morphology.

However, in general it is not sufficient to treat properties within effective medium theories [28] that relate heterogeneous systems to the properties of a homogenized “bulk” reference system. On nanometer-sized length scales matter behaves fundamentally different than on macroscopic length scales characteristic for bulk systems. In the case of lattice thermal conductivity for instance novel aspects like phonon confinement and additional phonon boundary scattering at interfaces have to be considered carefully on the nanoscale [25].

The interpretation of macroscopic, mechano-elastic experiments [11, 13, 31] to obtain the elastic moduli of the nanostructured Si-skeleton in pSi is similarly challenging. Macroscopic deformation experiments can be analyzed by means of finite element calculations that include the microscopic properties of the Si-skeleton as adjustable parameters. However, the implementation of the complex sample topology is an obvious obstacle to overcome.

This study does not follow the approach to determine the elastic properties of the pSi-skeleton indirectly from macroscopic measurements. In contrast, it utilizes inelastic thermal neutron scattering as a microscopic probe to determine the elastic moduli directly. The neutron scattering experiments elucidate the dispersion for phonons with wavelengths smaller than 2 nm that is well below the structuring length scale of pSi ( $\phi \approx 50\%$ ,  $R \approx 4 \text{ nm}$ ). An analysis of this dispersion within the framework of Born-Karman models allows inferring sound velocities in the Si-skeleton and subsequently the differences between bulk and nanostructure elasticity.

Fig. 5 exhibits the *bona-fide* indistinguishable phonon dispersions of pSi and

	$v_T^{[100]}$ [m/s]	$v_L^{[100]}$ [m/s]	$v_T^{[110]}$ [m/s]	$v_L^{[110]}$ [m/s]	$v_T^{[111]}$ [m/s]	$v_L^{[111]}$ [m/s]
bSi	5485 ± 29	8992 ± 18	5350 ± 39	8339 ± 48	5124 ± 37	10105 ± 35
pSi	5454 ± 40	8999 ± 16	5425 ± 52	8275 ± 50	4971 ± 79	10197 ± 41
bSi <sub>lit.</sub> [16, 17]	5844	8433	5844	9134	5094	9356
pSi/bSi	0.99	1.00	1.01	0.99	0.97	1.01

Table 1: Sound velocities for transverse and longitudinal phonons in bSi and pSi in the [100], [110], and [111] directions.

	$c_{11}$ [GPa]	$c_{12}$ [GPa]	$c_{44}$ [GPa]	$Y^{[100]}$ [GPa]	$Y^{[110]}$ [GPa]	$Y^{[111]}$ [GPa]
bSi	181 ± 1	68 ± 2	69 ± 1	145 ± 2	162 ± 1	169 ± 1
pSi	178 ± 2	73 ± 3	69 ± 1	135 ± 5	160 ± 2	170 ± 1.5

Table 2: Elastic moduli and uniaxial Young moduli for pSi and bSi as obtained from inelastic thermal neutron scattering experiments.

bSi for longitudinal and transverse phonons (symbols) along the high symmetry directions  $\overline{\Gamma L}$ ,  $\overline{\Gamma K}$  and  $\overline{\Gamma X}$ . The dashed lines represent data modeling according to Eqn. 1. An excellent agreement between data and the non-linear least squares approximation of Eqn. 1 is evident.

Tab. 1 lists sound velocities for pSi and bSi, which are calculated with Eqn. 2 using the optimized model parameters  $D_i$ . The sound velocities in the pSi-skeleton with 8 nm wide pores and bSi differ by less than 1% in average. The experimentally estimated sound velocities in bSi however deviate systematically by 5 - 10% from accepted literature values. This systematic error in the sound velocities forbids the discussion of the elastic moduli in terms of absolute values but does not affect not the direct comparison between pSi and bSi.

Components of the stiffness tensor  $c_{ij}$  and uniaxial Young moduli for pSi and bSi in Tab. 2 are derived with Eqn. 3. These results refine previous estimates in Ref. [16] for the effect of nanostructuring on the microstructural elastic properties of Si. Elastic moduli in pSi are reduced in average by less than 5% compared to bSi. Given the fairly conservative error estimates, one is indeed inclined to dispute any effect of nanostructuring on the elastic properties at all.

phonon-softening refers to the reduction of a phonon group velocity ,e. g., upon approaching a phase transition, a characteristic temperature or system size. In this sense, Wingert and Yang *et al.* [40, 42] report reduced elastic moduli that correspond via Eqn. 3 to soft phonon modes for Si nanotubes smaller than  $t_{NT} = 25$  nm in diameter [40] or Si nanoribbons with a surface to volume ratio  $S/V > 0.11$  nm<sup>-1</sup> [42].

In analogy with the nanotubes and -ribbons, one can readily characterize pSi by a locally defined, averaged pore-wall thickness  $t$  or the well-defined surface-to-volume ratio  $S/V$ . A simple geometrical model [16] allows estimating  $t$  from porosity and average pore radius. Surface-to-volume ratios can be extracted from the BET-analysis and the Si density  $\rho$ .

With values of  $t \approx 2$  nm  $< t_{NT}$  and  $S/V = A * \rho \approx 0.366$  nm<sup>-1</sup>  $> 0.11$  nm<sup>-1</sup> both quantities imply phonon-softening in pSi. However, no indications are found in the thermal neutron scattering experiments that indicate an influence

of nanostructuring on the phonon dispersion. Whether this difference between pSi and Si nanotubes and nanoribbons relates to the more complex, not-simply connected topology of pSi or the heavily disordered pore array is a fascinating question that remains unanswered and requires further experimental and theoretical studies beyond the scope of this work.

But as a matter of fact, this result puts a practical limit on the minimum thermal conductivity for anodized pSi membranes. Excluding unrealistic approaches like phonon dispersion engineering, nanostructuring induced phonon-softening appears as prerequisite to beat the so-called amorphous limit [6] of  $\kappa_{ph} = 0.1 \text{ Wm}^{-1}\text{K}^{-1}$  in pSi. In retrospective of the presented results, this necessitates samples with even higher porosity and smaller structural feature sizes, samples whose mechanical stability cannot be guaranteed.

It appears in order, to conclude this section with a brief review of results on phonon-softening in pSi as presented in Ref. [16]. There, Hofmann *et al.* study phonons with wavelengths between 2 nm and 10 nm to determine the elastic properties of pSi. Assuming to probe dominantly the properties of the pSi-skeleton a sizable phonon-softening in the range  $c_{ij}^{bSi} > c_{ij}^{pSi} > 0.75c_{ij}^{bSi}$  is inferred from scattering experiments. These results are clearly refined within the present study.

The cold neutron scattering experiments presented in Ref. [16] start the transition from microscopic probes like thermal neutron scattering to macroscopic probes like acoustic transmission spectroscopy. This troubling and admonishing tale of length scale dependent experimental results is unfortunately not new and known from diffusion experiments in confinement [8, 21] where different probes seemingly give different answers to the same question.

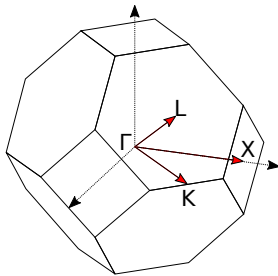


Figure 4: (Color online) First Brillouin zone of a fcc lattice: Dotted Arrows mark the cubic  $\{100\}$  directions. Red arrows show the high symmetry directions  $\overline{\Gamma L}$ ,  $\overline{\Gamma K}$  and  $\overline{\Gamma X}$ .

#### 4. Conclusion and Outlook

The inelastic neutron scattering studies presented in this article and in Ref. [16] are first steps towards a thorough understanding of the influence of nanostructuring on the phonon dynamics in phonon-softening silicon. Nanostructuring on sub-10 nanometer length scales does not have an effect on the

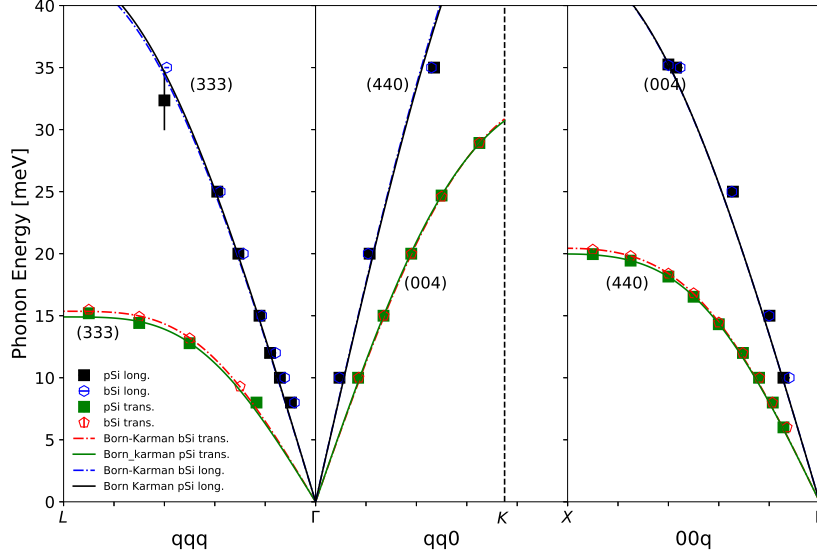


Figure 5: (Color online) Dispersion of longitudinal and transverse phonons in bSi (open symbols) and in porous silicon (filled symbols) along high symmetry directions  $[100](\bar{\Gamma}L)$ ,  $[110](\bar{\Gamma}K)$  and  $[111](\bar{\Gamma}X)$ : Labels indicate the Bragg reflection at which the phonons were measured. Colored lines (dashed, solid) represent Born-Karman approximations of the different dispersion branches.

phonon dispersion. In contrast to Si nanoribbons and nanotubes, no sizable phonon-softening in pSi is observed in the inelastic neutron scattering experiments.

Macroscopic thermal conductivity measurements evidence a strong effect of nanostructuring on phonon scattering rates in pSi. Deeper insights are expected from studies that probe the phonon life times respectively the scattering rates of phonons in structured silicon. Neutron resonance spin-echo spectroscopy appears as appropriate scattering technique to gain these insights [14]. It is however experimentally very challenging and comes along with new demands for sample quality and quantity. So this topic is left for now, with the prospect of tempting studies ahead.

### Acknowledgment

We thank FRM II for beamtime at the thermal triple-axis spectrometer PUMA and the granted experimental support.

- [1] Aliev, G. N., Goller, B., Snow, P. A., 2011. Elastic properties of porous silicon studied by acoustic transmission spectroscopy. Journal of Applied

- Physics 110 (4), 043534.  
URL <http://scitation.aip.org/content/aip/journal/jap/110/4/10.1063/1.3626790>
- [2] Andrews, G. T., Polomska, A. M., Vazsonyi, E., Volk, J., 2007. Brillouin light scattering from porous silicon films and multilayers. *physica status solidi (a)* 204 (5), 1372–1377.  
URL <http://dx.doi.org/10.1002/pssa.200674344>
- [3] Ashcroft, N., Mermin, N., 1976. *Solid State Physics*. HRW international editions. Holt, Rinehart and Winston.  
URL <https://books.google.de/books?id=oXIfAQAMAAJ>
- [4] Barrett, E. P., Joyner, L. G., Halenda, P. P., 01 1951. The determination of pore volume and area distributions in porous substances. i. computations from nitrogen isotherms. *Journal of the American Chemical Society* 73 (1), 373–380.  
URL <http://dx.doi.org/10.1021/ja01145a126>
- [5] Brunauer, S., Emmett, P. H., Teller, E., 02 1938. Adsorption of gases in multimolecular layers. *Journal of the American Chemical Society* 60 (2), 309–319.  
URL <http://dx.doi.org/10.1021/ja01269a023>
- [6] Cahill, D. G., Watson, S. K., Pohl, R. O., 09 1992. Lower limit to the thermal conductivity of disordered crystals. *Physical Review B* 46 (10), 6131–6140.  
URL <https://link.aps.org/doi/10.1103/PhysRevB.46.6131>
- [7] Canham, L., 2014. *Handbook of Porous Silicon*. Handbook of Porous Silicon. Springer International Publishing.  
URL <https://books.google.de/books?id=pCrZoAEACAAJ>
- [8] Chmelik, C., Enke, D., Galvosas, P., Gobin, O., Jentys, A., Jobic, H., Kärger, J., Krause, C. B., Kullmann, J., Lercher, J., Naumov, S., Ruthven, D. M., Titze, T., 2011. Nanoporous glass as a model system for a consistency check of the different techniques of diffusion measurement. *ChemPhysChem* 12 (6), 1130–1134.  
URL <https://doi.org/10.1002/cphc.201100072>
- [9] Coasne, B., Grosman, A., Ortega, C., Simon, M., 06 2002. Adsorption in noninterconnected pores open at one or at both ends: A reconsideration of the origin of the hysteresis phenomenon. *Physical Review Letters* 88 (25), 256102–.  
URL <http://link.aps.org/doi/10.1103/PhysRevLett.88.256102>
- [10] Enniful, H. R. N. B., Schneider, D., Hoppe, A., König, S., Fröba, M., Enke, D., Valiullin, R., 2019. Comparative gas sorption and cryoporometry study of mesoporous glass structure: Application of the serially connected

- pore model. *Frontiers in Chemistry* 7, 230.  
 URL <https://www.frontiersin.org/article/10.3389/fchem.2019.00230>
- [11] Gor, G. Y., Bertinetti, L., Bernstein, N., Hofmann, T., Fratzl, P., Huber, P., 2015. Elastic response of mesoporous silicon to capillary pressures in the pores. *Applied Physics Letters* 106 (26), 261901.  
 URL <http://scitation.aip.org/content/aip/journal/apl/106/26/10.1063/1.4923240>
- [12] Goupil, C., Ouerdane, H., Zabrocki, K., Seifert, W., Hinsche, N. F., Müller, E., 2016. *Thermodynamics and Thermoelectricity*. Wiley-VCH Verlag GmbH & Co. KGaA, pp. 1–74.  
 URL <http://dx.doi.org/10.1002/9783527338405.ch1>
- [13] Grosman, A., Puibasset, J., Rolley, E., 2015. Adsorption-induced strain of a nanoscale silicon honeycomb. *EPL (Europhysics Letters)* 109 (5), 56002.  
 URL <http://stacks.iop.org/0295-5075/109/i=5/a=56002>
- [14] Habicht, K., 2017. *Neutron-resonance spin-echo spectroscopy: A high resolution look at dispersive excitations*. Habilitationsschrift Universität Potsdam.
- [15] Hofmann, T., Kumar, P., Enderle, M., Wallacher, D., 02 2013. Growth of highly oriented deuterium crystals in silicon nanochannels. *Physical Review Letters* 110 (6), 065505–.  
 URL <http://link.aps.org/doi/10.1103/PhysRevLett.110.065505>
- [16] Hofmann, T., Wallacher, D., Toft-Petersen, R., Ryll, B., Reehuis, M., Habicht, K., 5 2017. Phonons in mesoporous silicon: The influence of nanostructuring on the dispersion in the debye regime. *Microporous and Mesoporous Materials* 243, 263–270.  
 URL <http://www.sciencedirect.com/science/article/pii/S1387181117300641>
- [17] Hopcroft, M., Nix, W., Kenny, T., April 2010. What is the young’s modulus of silicon? *Microelectromechanical Systems, Journal of* 19 (2), 229–238.
- [18] Hopkins, P. E., Phinney, L. M., Rakich, P. T., Olsson, R. H., El-Kady, I., 2010. Phonon considerations in the reduction of thermal conductivity in phononic crystals. *Applied Physics A* 103 (3), 575–579.  
 URL <http://dx.doi.org/10.1007/s00339-010-6189-8>
- [19] Jonson, M., Mahan, G. D., 05 1980. Mott’s formula for the thermopower and the wiedemann-franz law. *Physical Review B* 21 (10), 4223–4229.  
 URL <https://link.aps.org/doi/10.1103/PhysRevB.21.4223>
- [20] Kim, W., Wang, R., Majumdar, A., 2007. Nanostructuring expands thermal limits. *Nano Today* 2 (1), 40–47.

- URL <http://www.sciencedirect.com/science/article/pii/S174801320770018X>
- [21] Kondrashova, D., Lauerer, A., Mehlhorn, D., Jobic, H., Feldhoff, A., Thommes, M., Chakraborty, D., Gommers, C., Zecevic, J., de Jongh, P., Bunde, A., Kärger, J., Valiullin, R., 01 2017. Scale-dependent diffusion anisotropy in nanoporous silicon. *Scientific Reports* 7, 40207 EP –.  
URL <http://dx.doi.org/10.1038/srep40207>
- [22] Kondrashova, D., Valiullin, R., 2013. Improving structural analysis of disordered mesoporous materials using nmr cryoporometry. *Microporous and Mesoporous Materials* 178, 15–19.  
URL <http://www.sciencedirect.com/science/article/pii/S1387181113001728>
- [23] LaLonde, A. D., Pei, Y., Wang, H., Jeffrey Snyder, G., 2011. Lead telluride alloy thermoelectrics. *Materials Today* 14 (11), 526–532.  
URL <http://www.sciencedirect.com/science/article/pii/S1369702111702784>
- [24] Lorensen, W. E., Cline, H. E., 1987. Marching cubes: A high resolution 3D surface construction algorithm. In: *Proceedings of the 14th Annual Conference on Computer Graphics and Interactive Techniques. SIGGRAPH '87*. ACM, New York, NY, USA, pp. 163–169.  
URL <http://doi.acm.org/10.1145/37401.37422>
- [25] Minnich, A., Chen, G., 2007. Modified effective medium formulation for the thermal conductivity of nanocomposites. *Applied Physics Letters* 91 (7), 073105.  
URL <http://scitation.aip.org/content/aip/journal/apl/91/7/10.1063/1.2771040>
- [26] Miyata, H., Suzuki, T., Fukuoka, A., Sawada, T., Watanabe, M., Noma, T., Takada, K., Mukaide, T., Kuroda, K., 2004. Silica films with a single-crystalline mesoporous structure. *Nature Materials* 3 (9), 651–656.  
URL <https://doi.org/10.1038/nmat1184>
- [27] Mizuno, H., Mossa, S., Barrat, J.-L., 2015. Beating the amorphous limit in thermal conductivity by superlattices design. *Scientific Reports* 5 (1), 14116.  
URL <https://doi.org/10.1038/srep14116>
- [28] Nan, C.-W., 1993. Physics of inhomogeneous inorganic materials. *Progress in Materials Science* 37 (1), 1–116.  
URL <http://www.sciencedirect.com/science/article/pii/S0079642593900045>
- [29] Nolas, G. S., Morelli, D. T., Tritt, T. M., 2019/10/03 1999. Skutterudites: A phonon-glass-electron crystal approach to advanced thermoelectric energy conversion applications. *Annual Review of Materials Science* 29 (1),

89–116.

URL <https://doi.org/10.1146/annurev.matsci.29.1.89>

- [30] Pei, Y., Wang, H., Snyder, G. J., 2012. Thermoelectric materials: Band engineering of thermoelectric materials (adv. mater. 46/2012). *Advanced Materials* 24 (46), 6124–6124.  
URL <http://dx.doi.org/10.1002/adma.201290290>
- [31] Rolley, E., Garroum, N., Grosman, A., 02 2017. Using capillary forces to determine the elastic properties of mesoporous materials. *Physical Review B* 95 (6), 064106–.  
URL <https://link.aps.org/doi/10.1103/PhysRevB.95.064106>
- [32] Ryll, B., Schmitz, A., de Boor, J., Franz, A., Whitfield, P. S., Reehuis, M., Hoser, A., Müller, E., Habicht, K., Fritsch, K., 01 2018. Structure, phase composition, and thermoelectric properties of ybxco4sb12 and their dependence on synthesis method. *ACS Applied Energy Materials* 1 (1), 113–122.  
URL <https://doi.org/10.1021/acsaem.7b00015>
- [33] Sailor, M., 2012. *Porous Silicon in Practice: Preparation, Characterization and Applications*. Wiley.  
URL <https://books.google.de/books?id=QIJMWP41GMS>
- [34] Schneider, D., Valiullin, R., 07 2019. Capillary condensation and evaporation in irregular channels: Sorption isotherm for serially connected pore model. *The Journal of Physical Chemistry C* 123 (26), 16239–16249.  
URL <https://doi.org/10.1021/acs.jpcc.9b03626>
- [35] Seol, J. H., Barth, D. S., Zhu, J., C'oso, D., Hippalgaonkar, K., Lim, J., Han, J., Zhang, X., Majumdar, A., 2017/10/12 2017. Tunable thermal conductivity in mesoporous silicon by slight porosity change. *Applied Physics Letters* 111 (6), 063104.  
URL <http://dx.doi.org/10.1063/1.4997747>
- [36] Shirane, G., Shapiro, S., Tranquada, J., 2002. *Neutron Scattering with a Triple-Axis Spectrometer: Basic Techniques*. Cambridge University Press.  
URL <https://books.google.de/books?id=agc8GeLZ-joc>
- [37] Slack, G. A., 1997. Design concepts for improved thermoelectric materials. *MRS Proceedings* 478, 47.  
URL <https://www.cambridge.org/core/article/design-concepts-for-improved-thermoelectric-materials/B2335260AA3F88740F973E6C76531807>
- [38] Snyder, G. J., Toberer, E. S., 02 2008. Complex thermoelectric materials. *Nature Publishing Group* 7 (2), 105–114.  
URL <http://dx.doi.org/10.1038/nmat2090>

- [39] Sobolev, O., Park, J. T., 2015. Puma: Thermal three axes spectrometer. *Journal of large-scale research facilities JLSRF* 1 (A13), 1–4.
- [40] Wingert, M. C., Kwon, S., Hu, M., Poulikakos, D., Xiang, J., Chen, R., 04 2015. Sub-amorphous thermal conductivity in ultrathin crystalline silicon nanotubes. *Nano Letters* 15 (4), 2605–2611.  
URL <http://dx.doi.org/10.1021/acs.nanolett.5b00167>
- [41] Witting, I. T., Chasapis, T. C., Ricci, F., Peters, M., Heinz, N. A., Hautier, G., Snyder, G. J., 2019/10/04 2019. The thermoelectric properties of bismuth telluride. *Advanced Electronic Materials* 5 (6), 1800904.  
URL <https://doi.org/10.1002/aelm.201800904>
- [42] Yang, L., Yang, Y., Zhang, Q., Zhang, Y., Jiang, Y., Guan, Z., Gerboth, M., Yang, J., Chen, Y., Greg Walker, D., Xu, T. T., Li, D., 2016. Thermal conductivity of individual silicon nanoribbons. *Nanoscale* 8 (41), 17895–17901.  
URL <http://dx.doi.org/10.1039/C6NR06302K>
- [43] Zdetsis, A. D., Wang, C. S., 03 1979. Lattice dynamics of ge and si using the born-von karman model. *Physical Review B* 19 (6), 2999–3003.  
URL <https://link.aps.org/doi/10.1103/PhysRevB.19.2999>
- [44] Zhang, X. G., 01 2004. Morphology and formation mechanisms of porous silicon. *Journal of The Electrochemical Society* 151 (1), C69–C80.  
URL <http://jes.ecsdl.org/content/151/1/C69>